© 2021. Published by The Company of Biologists Ltd | Journal of Cell Science (2021) 134, jcs244384. doi:10.1242/jcs.244384

RESEARCH ARTICLE

Rab11FIP1 maintains Rab35 at the intercellular bridge to promote actin removal and abscission

Nicholas V. G. Iannantuono[1] and Gregory Emery[1,2,*]

ABSTRACT

Cytokinesis occurs at the end of mitosis/meiosis wherein the cytoplasms of daughter cells are separated. Before abscission, an intercellular bridge containing the remaining furrowing machinery, mitotic spindle and actin cytoskeleton connects the two daughter cells. To remove this actin and allow for the separation of daughter cells, Rab35 vesicles, loaded with the actin oxidizer MICAL1 and the inositol polyphosphate 5-phosphatase OCRL, are recruited to the midbody in a fine-tuned spatiotemporal manner. However, importantly, the means by which these vesicles are recruited is currently unclear. Here, we demonstrate that Rab11FIP1 is recruited to the midbody after Rab35 to scaffold it at the bridge and maintain Rab35 in this region. In the absence of Rab11FIP1, Rab35 dramatically drops from the midbody, inducing defects, such as cytokinetic delays and binucleation due to actin overaccumulation at the intercellular bridge, which can be rescued with Latrunculin A treatment. Importantly, we show that Rab11FIP1 is critical for Rab35 function in actin removal prior to cytokinesis.

This article has an associated First Person interview with the first author of the paper.

KEY WORDS: Rab11FIP, Rab35, Abscission, Actin, Cytokinesis, Vesicular trafficking

INTRODUCTION

Cytokinesis occurs at the end of mitosis/meiosis wherein the cytoplasms of daughter cells are separated, giving rise to two independent cells (Frémont and Echard, 2018; Gatta and Carlton, 2019; Holder et al., 2019; Peterman and Prekeris, 2019; Vietri et al., 2020). Just before this abscission, daughter cells remain attached by an intercellular bridge (ICB) that contains the remnants of the furrowing machinery and an array of cytoskeleton components, including the mitotic microtubule spindle and actin cytoskeleton (Frémont and Echard, 2018; Peterman and Prekeris, 2019; Echard, 2008; Klinkert and Echard, 2016; Kouranti et al., 2006). The removal of this filamentous actin prior to abscission has been a field of active research over the past decade as its ineffective removal has been tied to deficient abscission, which in turn has been linked with diseases such as Lowe syndrome and cancer (Carim et al., 2019; Festa et al., 2019; Bökenkamp and Ludwig, 2016; Erneux et al., 2016; Cauvin et al., 2016; Sugimoto et al., 2014; Vicinanza et al., 2011; Chesneau et al., 2012).

In fact, the removal of this actin has been linked with very precise modulation of the ICB lipid composition by the small GTPase Rab35 (Frémont and Echard, 2018; Kouranti et al., 2006; Dambournet et al., 2011). Rabs are small GTPases that regulate different stages of intracellular trafficking. These proteins oscillate between inactive and active states, in which they are thought to bind downstream effectors and modulate cellular functions pertaining to trafficking, such as vesicle fusions, motility and docking. Rab35 has been linked to several functions, most notably fast recycling to the plasma membrane (Klinkert and Echard, 2016; Cauvin et al., 2016; Chesneau et al., 2012), but most recently its linchpin role in cytokinesis has been at the forefront. Indeed, Rab35 has been shown to recruit both MICAL1 (Frémont et al., 2017) and OCRL (Cauvin et al., 2016; Dambournet et al., 2011; Frémont et al., 2017; Kouranti et al., 2006). MICAL1 is an actin oxidizing enzyme that causes actin depolymerization, whereas OCRL is a PI(4,5)P2 phosphatase that helps to detach any remaining furrowing machinery and actin nucleators. This alleviates the barrier of actin that has been shown to physically impede ESCRT-III polymerization; however, the means by which Rab35 is specifically recruited after telophase to the ICB is unclear.

Of note, as mentioned earlier, Rabs act through different effectors, and a specific group of Rab11 effectors, namely Rab11FIPs (henceforth named FIPs), have been well characterized as linking Rab11 vesicles with molecular motors (Baetz and Goldenring, 2013; Carson et al., 2013; de Renzis et al., 2002; Eva et al., 2010; Fan et al., 2003, 2004; Jin and Goldenring, 2006; Jing et al., 2010; Lall et al., 2015; Li et al., 2014a,b; Lindsay and McCaffrey, 2005, 2004; Moore et al., 2004; Nedvetsky et al., 2007; Neto et al., 2013; Peden et al., 2004; Rainero et al., 2012; Sechi et al., 2014; Willenborg et al., 2011). FIPs come in two classes, namely the FIP1 (also known as Rab11FIP1), FIP2 (Rab11FIP2) and FIP5 (Rab11FIP5) of the class I FIPs, and FIP3 (Rab11FIP3) and FIP4 (Rab11FIP4) of the class II FIPs. Class I FIPs have been associated with various trafficking events, such as the recycling of different proteins to the plasma membrane, e.g. GLUT4-containing vesicles (Bruno et al., 2016), the water channel protein AQP2 (Nedvetsky et al., 2007), the chemokine receptor CXCR2 (Fan et al., 2003, 2004) and different integrin complexes, most notably α5β1 (Eva et al., 2010; Hwang et al., 2017; Rainero et al., 2012). As for Class II FIPs, both FIP3 and FIP4 have been shown to play key roles during cytokinesis in which they couple Rab11 and Arf6 at the ICB during cell division (Ai and Skop, 2009; Chesneau et al., 2012; Takahashi et al., 2011). Of note, mammalian Class I FIPs have not currently been formally linked to cytokinesis. Nevertheless, we have shown in a previous study that the sole *Drosophila* Class I FIP, Rip11, localizes to the ICB and its depletion leads to cytokinesis defects in a Rab11-independent manner (Laflamme et al., 2017).

[1]Vesicular Trafficking and Cell Signalling Research Unit, Institute for Research in Immunology and Cancer (IRIC), Université de Montréal, P.O. Box 6128, Downtown station, Montréal, Québec H3C 3J7, Canada. [2]Department of Pathology and Cell Biology, Faculty of Medicine, Université de Montréal, Montréal, Québec H3C 3J7, Canada.

*Author for correspondence (gregory.emery@umontreal.ca)

G.E., 0000-0002-6874-6875

Handling Editor: Mahak Sharma
Received 21 January 2020; Accepted 20 May 2021

Journal of Cell Science (2021) 134, jcs244384. doi:10.1242/jcs.244384

Here, we present our data that strongly suggest that FIP1 acts as an atypical molecular tether that serves to maintain Rab35 levels elevated in the ICB prior to abscission, and that its depletion leads to a dramatic drop-off of Rab35. We show that FIP1 depletion leads to similar phenotypes to the depletion of Rab35, including cellular binucleation, cytokinesis delays and polarity inversion in three-dimensional cultures due to overaccumulation of actin and subsequent cytokinesis failure. Finally, we show that FIP1 depletion can be rescued entirely with a low dose of Latrunculin A to artificially reduce actin levels, similar to what was observed in Lowe syndrome patient cells.

RESULTS

FIP1 is required for timely cytokinesis completion

In order to examine the function of class I FIPs on mitosis, we first individually depleted the three FIPs of class I, hereafter named FIP1, FIP2 and FIP5, in U2OS cells (Fig. 1A). The knockdown of FIP1, FIP2 and FIP5 did not induce any overt phenotypes with regards to the cytoskeleton or cause any other gross morphological phenotypes (Fig. 1B). Nevertheless, a subtle (∼7%) but significant increase in binucleated cells could be observed in cells knocked down for FIP1 (Fig. 1C). Moreover, cumulative depletions of different FIPs never caused synergistic effects, always remaining at a similar binucleation to FIP1 depletion alone (Fig. S1A). It is of note that we could not measure binucleation in the triple knockdown as significant cell death was quickly induced over the first 3 days. Nevertheless, to ensure that this phenotype was not cell line specific, we performed FIP1 knockdown in a variety of different cell lines. Our results showed that in all cell lines, with the exception of HeLa cells, the silencing of FIP1 induced cell binucleation to varying degrees, with U2OS showing the most prominent effects (Fig. S1B).

We next sought to understand the mechanism by which cellular binucleation was induced. For this, we first examined the state of telophase cleavage ring furrowing, as unstable furrowing often leads to binucleation. We therefore monitored one of the major regulators of cytokinesis, the centralspindlin component MKLP1, the functions of which include tethering the mitotic spindle to the plasma membrane for proper formation of the midbody after telophase. Indeed, MKLP1 staining showed no observable differences between control and FIP1-depleted cells (Fig. S1C). Furthermore, we expressed the RhoA-binding-domain-of-anillin as a proxy for RhoA activation and localization and found no difference between control and FIP1-depleted cells (Fig. S1C). Upon closer examination, we observed that FIP1 depletion induced an increase in the percentage of cells bound by acetyl-tubulin-positive bridges (Fig. 1D), as well as a decrease in the amount of those bridges that displayed secondary ingressions (Fig. 1D). These results strongly suggest that FIP1 depletion causes an abscission delay. Indeed, our measurements of the time between telophase and mitotic spindle severing (Fig. 1E) indicate that control cells on average take 170 min to complete cytokinesis, whereas cells depleted for FIP1 require 328 min (Fig. 1E; Fig. S1D), indicating a cytokinesis delay. Long-term depletion of FIP5 yielded high cell death post 72 h, thus we excluded this protein from further analysis. As expected, knockdown of FIP2 did not induce a cytokinesis delay (Fig. 1E; Fig. S1D). To explore what might be causing this cytokinetic delay, we first examined the localization of FIP3, an important player in the delivery of $Rab11^+$ endosomes to the ICB, as well as the ESCRT-III component CHMP4B. Of note, whether looking at early recruitment to ICBs harboring no secondary ingressions, or looking at late ICBs displaying clear secondary ingressions, we could not observe any difference in the levels of FIP3 or CHMP4B, suggesting that FIP1 depletion does not impede the ability of these proteins to localize to the ICB (Fig. S1E). There are different isoforms of FIP1, namely FIP1A, FIP1B and FIP1C. Thus, we sought to determine which of these isoforms was required in cytokinesis. To this end, we established stable cell lines expressing GFP-FIP1A, GFP-FIP1B and GFP-FIP1C (Fig. 1F). It is of note that our siFIP1 targets the 3′ UTR, and thus, it does not affect the expression of our exogenous constructs. When these cells were subjected to FIP1 knockdown, FIP1B and FIP1C, but not FIP1A expression, rescued both binucleation and cytokinesis timing (Fig. 1G,H; Fig. S1D), suggesting that either FIP1B or FIP1C are redundantly required for timely cytokinesis completion.

FIP1B and FIP1C localize to the midbody, abscission site and daughter cell-cell interface during mitosis

As FIP1B and FIP1C rescue the binucleation and cytokinesis timing phenotypes observed during FIP1 knockdown, we investigated the specific localization of the different FIP1 isoforms (Fig. 2A) during mitosis using live-cell imaging on our stable cell lines. Both FIP1B and FIP1C localized to vesicular structures in most of interphase, whereas FIP1A demonstrated mostly cytoplasmic staining (Fig. 2B). Interestingly, neither A, B nor C showed any distinct localization during mitotic prophase, metaphase and anaphase. Upon entry into telophase, FIP1B localization moved drastically towards the extremity of the mitotic spindle between both daughter cells, a localization that remained stable throughout telophase progression until a sudden shift towards the middle of the spindle just before abscission, with a gradual pullback to the sides of the abscission site after abscission had occurred, as represented by the line scans below each image (Fig. 2B). FIP1C localization was very similar to that of FIP1B, as can be seen in Fig. 2B, wherein FIP1C localized to both extremities of the spindle during telophase and just after abscission. Upon entry into G1, both FIP1B and FIP1C had very similar localization. As for FIP1A, it remained cytoplasmic throughout mitosis and did not show specific localization to any clear mitotic component, be it the spindle or abscission site. These results suggest that FIP1B and FIP1C are recruited to the ICB during the end of mitosis.

Rab11FIP1 interacts with Rab35 via both its N and C terminus

As our results suggest that FIP1B and FIP1C have activity in cytokinesis, we sought to identify a cargo that they may be trafficking during this phase. To do this, we first examined the recently published Bio-ID interactome of FIP1 available in the Cell Map database (https://cell-map.org/; Fig. 3A). As expected, Rab11A was reported as the strongest hit. In addition, there are several proteins involved in endocytic recycling, such as STX7, STX6, RAB9a, CAV1 and RAB5A. Most interestingly, Rab35 was detected with a near perfect significance analysis of interactome (SAINT) score of 0.98, and this protein has recently been strongly tied to cytokinesis defects that are reminiscent of the phenotype we observed in FIP1 knockdown. As such, we examined FIP1 binding with Rab35. Firstly, we performed immunoprecipitations of exogenous constructs for each isoform of FIP1 using different Rabs as baits. As expected, all FIP1 isoforms interacted strongly with both Rab11a and Rab11b (Fig. 3B). Furthermore, we observed interaction between Rab35 and all three isoforms of FIP1. We also tested another known interacting Rab, Rab14 (Lall et al., 2015; Qi et al., 2013), despite it not appearing in the BioID analysis, and also observed interaction with all three isoforms of FIP1 (Fig. 3B).

Journal of Cell Science (2021) 134, jcs244384. doi:10.1242/jcs.244384

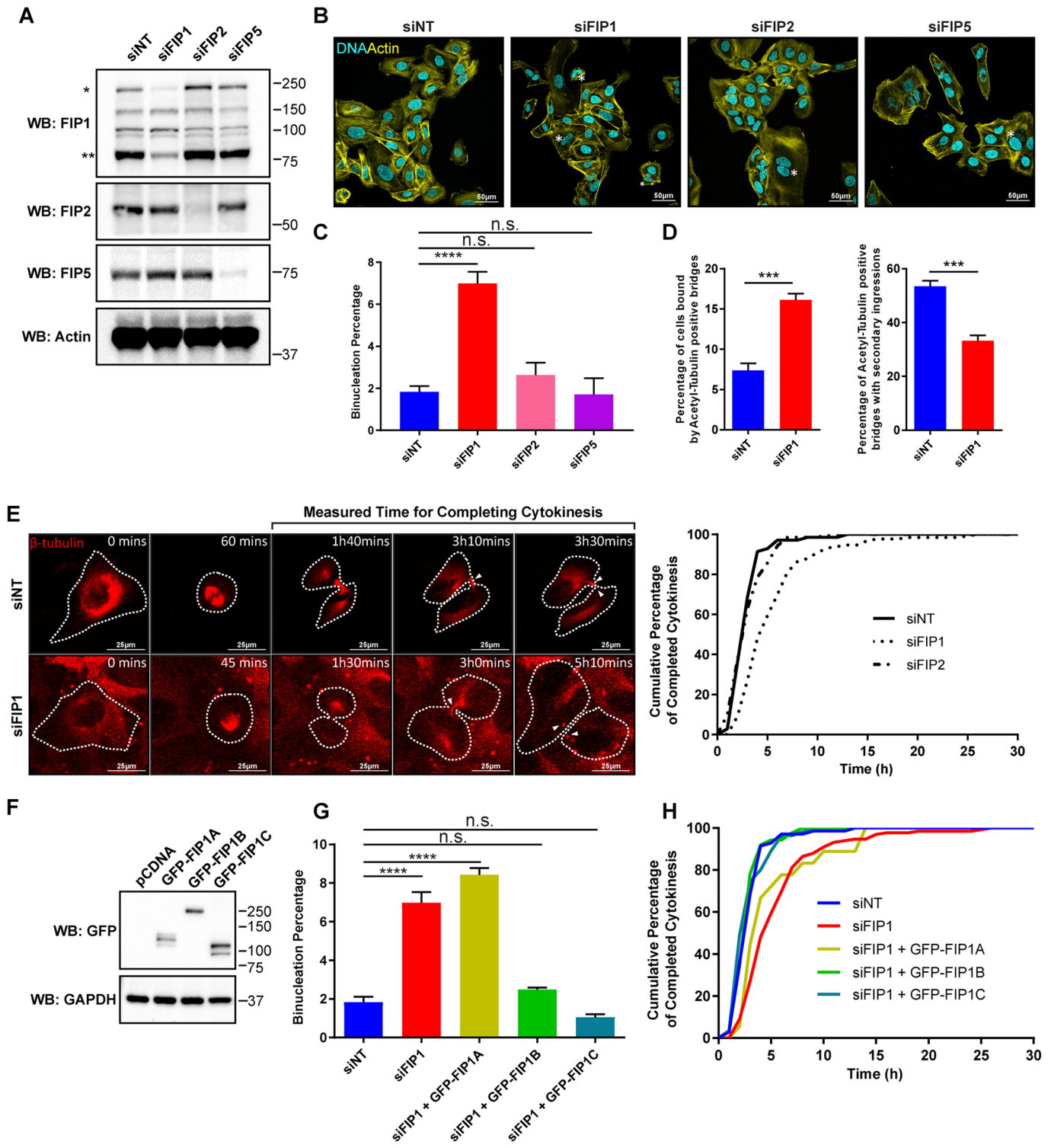

Fig. 1. FIP1 is required for timely cytokinesis completion. (A) Representative western blot showing indicated protein depletions. FIP1 antibody has non-specific bands and a single asterisk denotes FIP1B, and a double asterisk denotes FIP1C. (B) Representative images of cells depleted for FIP1, FIP2, and FIP5 stained for actin (yellow) and DNA (cyan). Binucleated cells are indicated with asterisks. (C) Quantification of average cellular binucleation. siNT, *n*=496; siFIP1, *n*=719; siFIP2, *n*=643; siFIP5, *n*=107. (D) Left: quantification of the percentage of cells bound by acetyl-tubulin-positive ICBs. siNT, *n*=1374; siFIP1, *n*=1731. Right: quantification of the percentage of cells bound by acetyl-tubulin-positive ICBs that show secondary ingressions. siNT, *n*=45; siFIP1, *n*=53. (E) Left: representative images of how cytokinesis timing was measured. Timing was measured as the time between the frame of telophase and the frame in which the mitotic spindle (indicated by the arrowheads) was severed. Cells were stained with SiR-tubulin (red), and dotted lines were added to the images to delineate the cell body. Right: quantification of cumulative cytokinesis timing for siNT (*n*=71), siFIP1 (*n*=133) and siFIP2 (*n*=72) over time. (F) Western blot showing expression of exogenous GFP-FIP1A, GFP-FIP1B and GFP-FIP1C constructs in stable cell lines. (G) Quantification of average cellular binucleation following rescue experiments. GFP-FIP1A, *n*=509; GFP-FIP1B, *n*=170; GFP-FIP1C, *n*=251. (H) Quantification of cumulative cytokinesis timing for rescue constructs. GFP-FIP1A, *n*=18; GFP-FIP1B, *n*=19; GFP-FIP1C, *n*=26. Data in C,D,G are presented as mean±s.e.m. ***P<0.001; ****P<0.0001; n.s., not significant (unpaired two-tailed Student's *t*-test).

Journal of Cell Science

Journal of Cell Science (2021) 134, jcs244384. doi:10.1242/jcs.244384

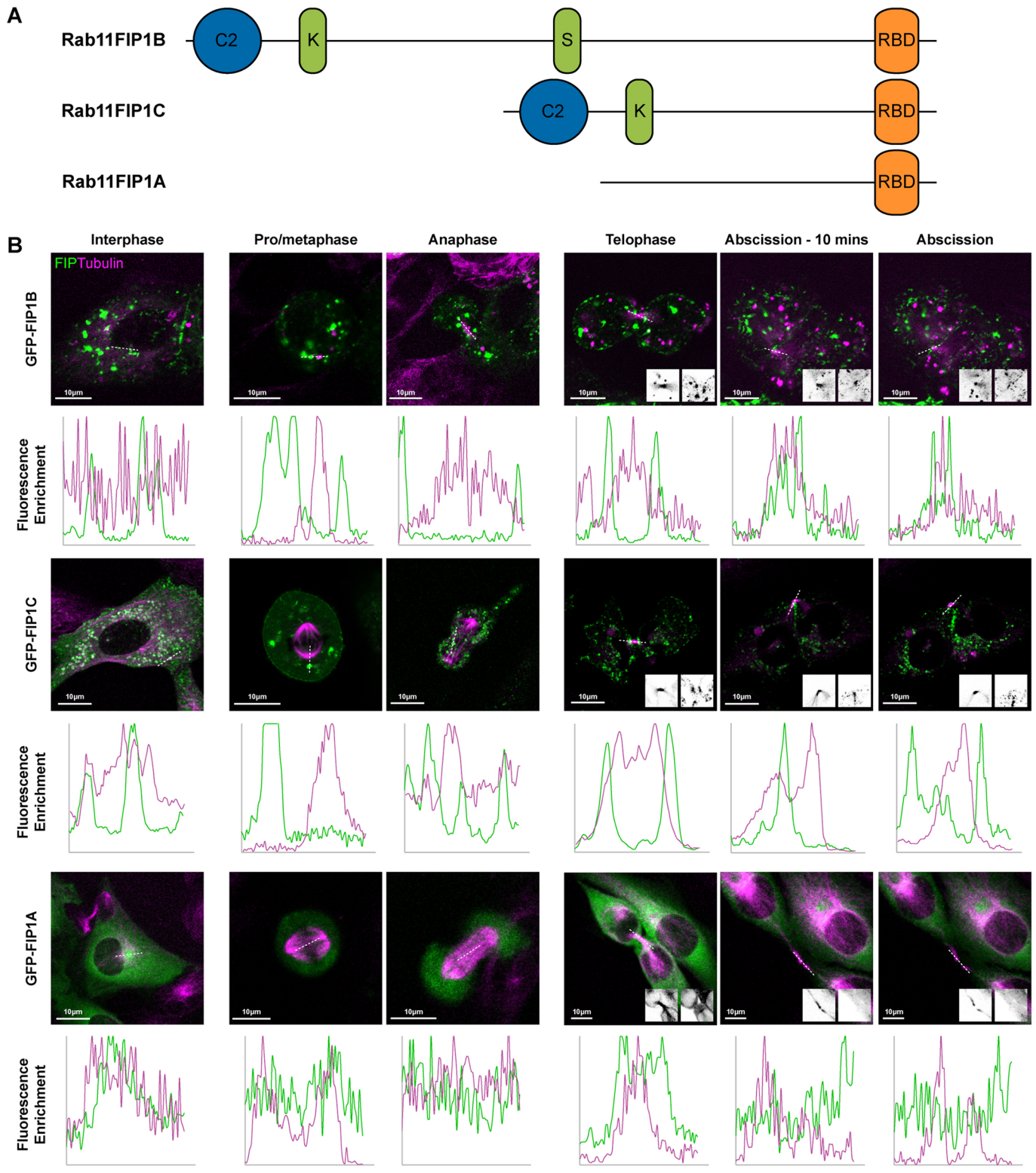

Fig. 2. FIP1B and FIP1C localize to the midbody, abscission site and daughter cell-cell interface during mitosis. (A) Schematic representation of FIP1 isoforms showing N-terminal C2 domains, lysine rich motif (K), serine-rich motif (S) and C-terminal Rab11-binding domain (RBD). (B) Still images of stable cell lines expressing either GFP-FIP1B, GFP-FIP1C or GFP-FIP1A progressing through the phases of mitosis, stained with SiR-tubulin (magenta) to observe tubulin and GFP-FIPs (green). Higher magnification black and white images of the spindle and FIP are in the lower corner of each merge. Line scans were drawn (as denoted by the dashed lines) to demonstrate the localization of normalized fluorescence intensity through the mitotic spindle as cells progress from telophase to cytokinesis.

Journal of Cell Science (2021) 134, jcs244384. doi:10.1242/jcs.244384

A

PROTEIN	SC	SAINT
RAB11A	143	1
STX7	99	1
RHOB	26.5	1
KRAS(Q61H)	26.5	1
RAB9A	21.5	1
RAB35	19	0.98
OCLN	14	0.99
STX6	13	1
ZFPL1	13	0.99
EBAG9	11.5	1
CAV1	11.5	1
MARCKS	12	0.96
LYN	11.5	0.95
LAMP2	11	0.96
RAB4A	10	0.95
FLOT1	9.5	0.94
LCK	9	0.91
CXADR	9	0.93
LAMTOR1	8.5	0.9
LAMP3	8.5	0.92
RAB5A	6	0.9

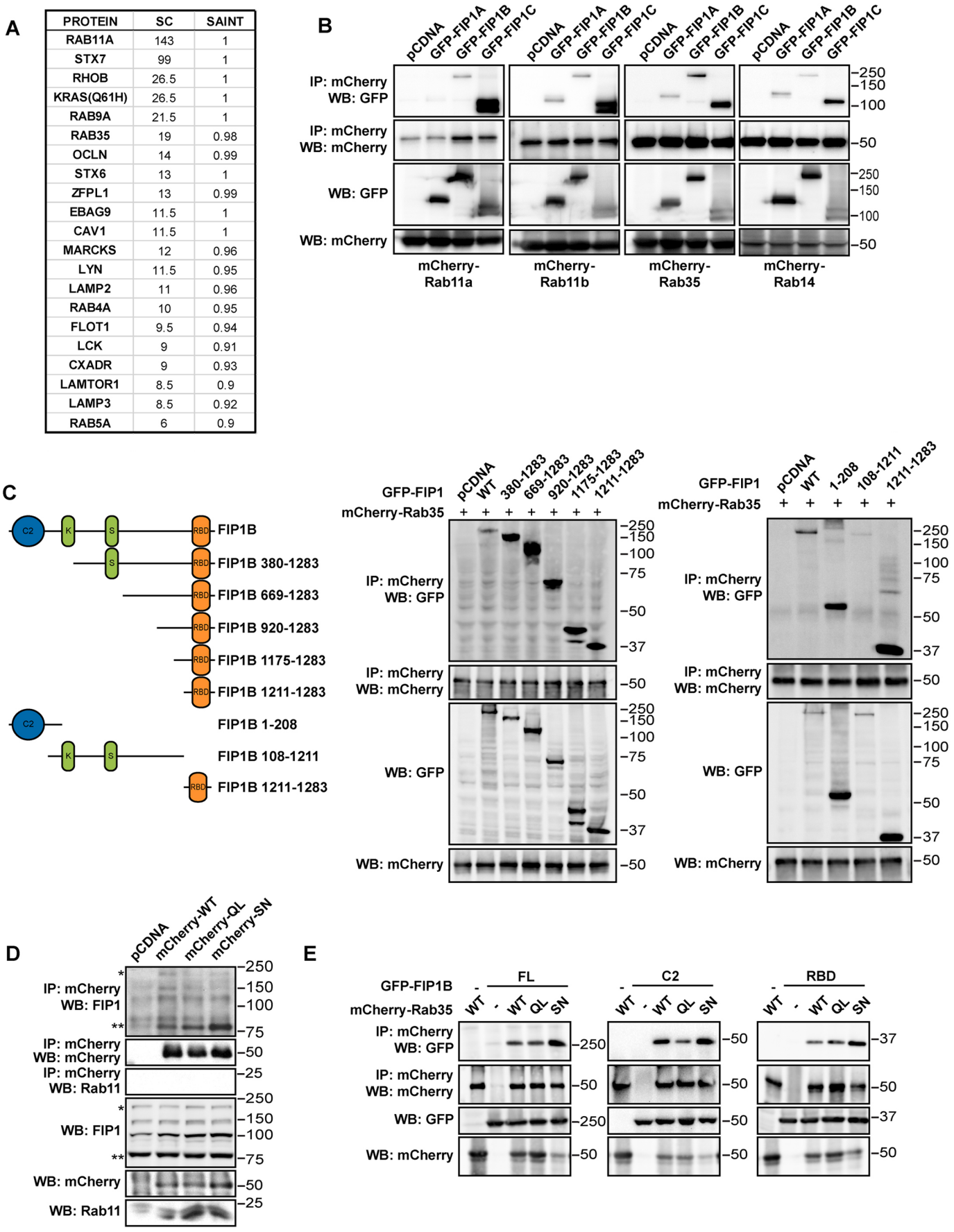

Fig. 3. See next page for legend.

Journal of Cell Science (2021) 134, jcs244384. doi:10.1242/jcs.244384

Fig. 3. Rab11FIP1 interacts with Rab35 via both its N and C terminus. (A) Summary table of the publicly available Bio-ID interactome dataset for FIP1 from Cell Map, showing average spectral counts (SC) and SAINT score for interactors. (B) Immunoprecipitation of indicated mCherry-Rabs with exogenous GFP-FIP1 isoforms. (C) Schematic representation of FIP1 constructs (left) used for immunoprecipitations (right) showing interactions between FIP1 N-terminal deletion constructs with mCherry-Rab35, as well as the interactions between the FIP1 N-terminal C2 domain, middle domain and C-terminal RBD domain with mCherry-Rab35. (D) Immunoprecipitation of endogenous FIP1 and Rab11 by mCherry-Rab35 wild type (WT), catalytically active mutant (QL) and dominant-negative (SN). The FIP1 antibody has non-specific bands and a single asterisk denotes FIP1B, and a double asterisk denotes FIP1C. (E) Immunoprecipitation of GFP-FIP1B full length, C2 domain or RBD domain by mCherry-Rab35 wild type (WT), catalytically active mutant (QL) and dominant-negative (SN).

Strikingly, in Fig. 1F and Fig. 3B, the FIP1C exogenous construct appeared as a double band, which interacted with both Rab11a and Rab11b, but only the upper band seemed to interact with Rab35 or Rab14. We also examined FIP1 interaction with a panel of other Rabs, namely Rab1a, Rab5, Rab6a, Rab10 and Rab13. When performing immunoprecipitations of either exogenous FIP1B or FIP1C, we could only observe interaction with exogenous Rab11 and Rab35 (Fig. S2A, left and right). As expected, binding between FIP1B/C and Rab11 was stronger than with Rab35. Next, we developed different N-terminal deletion constructs of FIP1B to map the domain of interaction with Rab35. As expected, the Rab11-binding domain (RBD) of FIP1 could interact with Rab35 (Fig. 3C, left), confirming previously published literature on the promiscuity of the FIP1 RBD (binding to Rab4 and Rab14) (Qi et al., 2013; Lall et al., 2015). Surprisingly, when we tested whether Rab35 could bind other domains of FIP1, we found that although binding to the central domain (108-1211) was barely detectable, Rab35 interacted strongly with the C2 domain of FIP1 (Fig. 3C, right). As the C2 domain is absent in FIP1A, we hypothesize that this binding might confer the specific activity of FIP1B and FIP1C to Rab35. This correlates with the temporal localization changes observed in FIP1B and FIP1C that are absent in FIP1A (Fig. 2B). Furthermore, as many studies and crystal structures have shown that FIPs form homodimers, we verified whether these two domains can dimerize with the full length of FIP1, and indeed, both the C2 and RBD could dimerize with full-length FIP1 (Fig. S2B), whereas the middle domain showed poor ability to dimerize with full-length FIP1. Crystal structures have shown that FIP1 RBD domains can dimerize (Lall et al., 2015) but it is unclear what function a C2 domain dimer might have. We next sought to determine whether FIP1 could act like a Rab35 effector. For this, we performed a similar experiment to that in Fig. 3B, in which we pulled down Rab35 wild type and looked at FIP1 binding, but this time we also used Rab35 catalytically active (QL) and dominant-negative (SN), and looked at the binding of endogenous FIP1. Interestingly, these results suggest that FIP1C isoform can bind to all variants of Rab35 but showed a preference for Rab35 dominant-negative (Fig. 3D). The binding between FIP1B and Rab35 wild type could also be observed; however, due to the high molecular weight and low expression of FIP1B relative to FIP1C, it was difficult to observe endogenous FIP1B binding to Rab35 (Fig. 3D). To this end, we sought to confirm these findings using overexpression conditions whereby both FIP1B and the C2 or RBD domains alone were pulled down by Rab35 wild type, QL or SN. These experiments showed that FIP1B and its domains all recapitulated the preference for Rab35SN observed with endogenous FIP1C (Fig. 3E). As both FIP1B and FIP1C contain identical C2 and RBD domains, we believe FIP1 might act as an atypical effector, preferring the dominant-negative form of this Rab GTPase (Fig. 3E). This parallels the function of IRSp53, which was very recently shown to also specifically bind the dominant-negative Rab35S22N and regulate Rab35 localization (Bisi et al., 2020). The discrepancy between entirely and partially exogenous binding (Fig. 3D,E) might suggest that strong expression of FIP proteins increases binding. Furthermore, the inverse experiment, whereby FIP1B and FIP1C was expressed and co-immunoprecipitated, showed binding to endogenous Rab11 as expected (Fig. S2C), but not to endogenous Rab35. This could be because this interaction only occurs in a subset of mitotic cells and with only a subset of the total FIP1 protein. As such, it would be difficult to observe in this direction.

Finally, as we observed interaction between Rab35 and different domains of FIP1 (Fig. 3C, right) in various overexpression and/or endogenous conditions (Fig. 3C-E; Fig. S2A), and as we and others have shown that FIP1 domains can dimerize (Fig. S2B), we sought to investigate whether we could observe direct binding between FIP1 domains and Rab35 *in vitro*. For this, we purified the His-RBD domain of FIP1 from bacteria and verified its binding with either empty, GTP-loaded or GDP-loaded Rab11 and Rab35. As expected, FIP1 RBD demonstrated a preference towards Rab11-GTP (Fig. S2D). Interestingly, although it can bind GTP-loaded Rab35, FIP1 RBD shows a clear preference towards the GDP-bound form of Rab35, suggesting that FIP1 RBD:Rab35 binding is direct. This is very reminiscent of IRSp53 preference towards Rab35-GDP, as well as our other data regarding Rab35SN. We also tested the ability of the C2 domain of FIP1 to bind Rab35 but we were unable to observe direct binding with the C2 domain in this context (Fig. S2E). This could be because of *in vitro* conditions not reflecting the cellular or lipidic environment of the C2:Rab35 interaction, lack of post-translational modifications or simply that the C2:Rab35 binding is not direct. Taken together, our results suggest that FIP1 activity in cytokinesis might be through Rab35 binding.

FIP1 binding to Rab35 is required for its proper localization during cytokinetic abscission

Our previous work demonstrated that the function of *Drosophila* FIP1 orthologue Rip11 was independent of its Rab11 binding. Here, we sought to discriminate whether FIP1 function in cytokinesis was via its Rab11 binding or its Rab35 binding. As we determined that, similar to other Rab binding, FIP1 could bind Rab35 via its RBD, we developed mutant constructs of the FIP1 RBD, namely Y1254S (which we published as being able to abrogate Rab11:Rip11 binding while retaining its cytokinesis function), the I1255E and D1256N mutants, which were shown to abrogate the RBD function, as well as an entire truncation of the RBD domain, and tested their ability to bind Rab35 and rescue the cytokinesis phenotypes we have observed. Indeed, as expected, all three mutant forms and the RBD truncation were completely unable to bind Rab11b (Fig. S3A). Surprisingly, all these mutant forms could bind Rab35 as strongly as the wild-type FIP1B. Although we could not demonstrate a direct interaction *in vitro* (Fig. S2E) between the C2 domain of FIP1 and Rab35, this result strongly suggested that in cells the C2 domain (Fig. 4A) can confer sufficient Rab35 binding. Furthermore, although this does not preclude the ability of the C2 domain of FIP1 to bind other Rabs, it strongly suggests that the C2 domain of FIP1 is unable to bind Rab11, as it is present in all of these constructs (Fig. S3A). As such, we established stable cell lines expressing different mutant constructs (Fig. 4B, upper) encompassing the C2 and RBD domains, as well as the RBD mutants, and verified their ability to rescue the FIP1 knockdown phenotype. By measuring cellular binucleation, our results indicate

Journal of Cell Science (2021) 134, jcs244384. doi:10.1242/jcs.244384

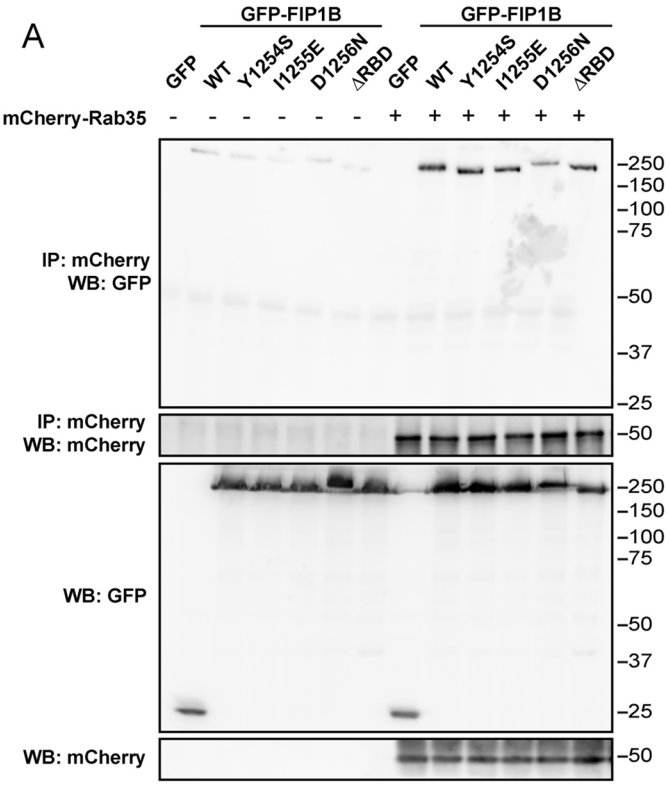

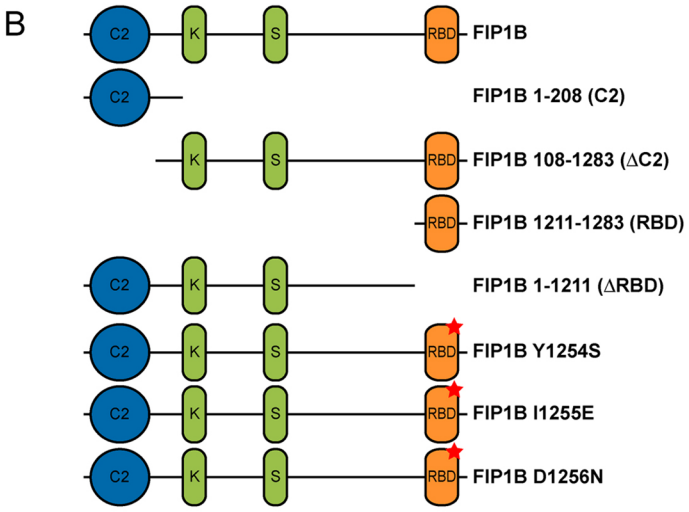

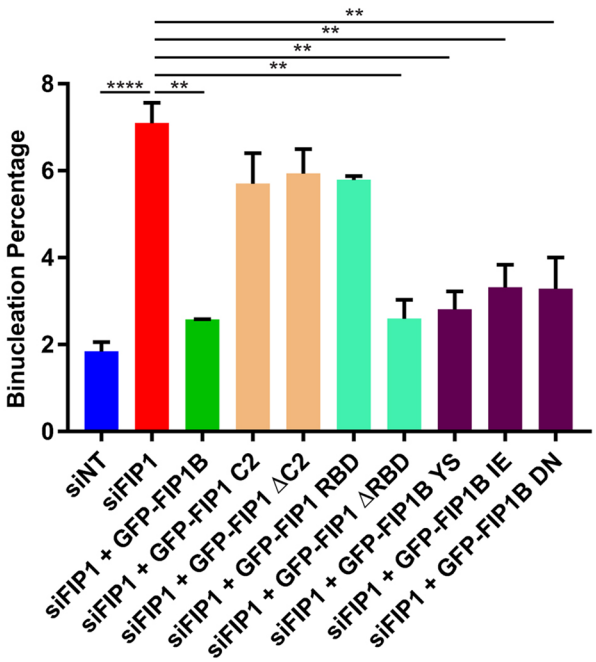

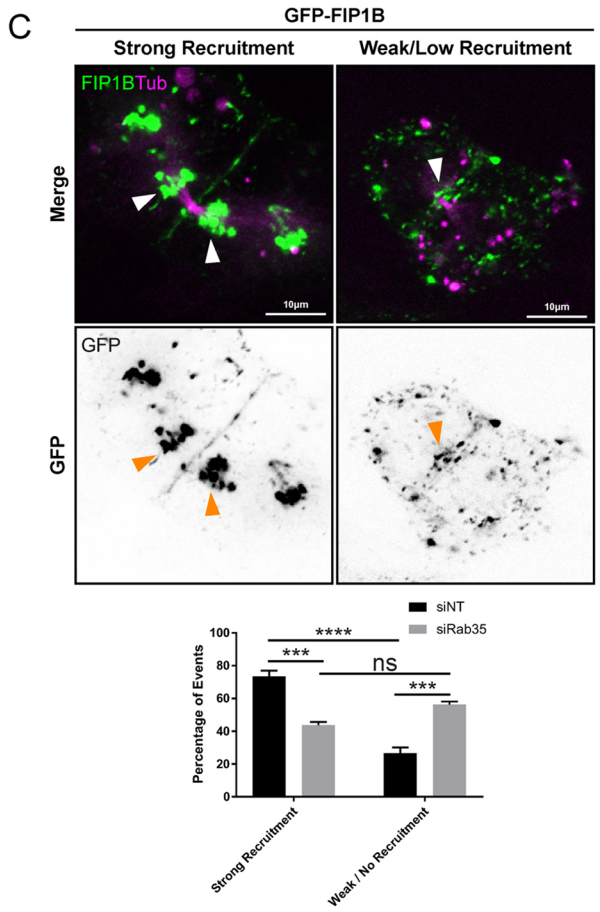

Fig. 4. See next page for legend.

Journal of Cell Science (2021) 134, jcs244384. doi:10.1242/jcs.244384

Fig. 4. FIP1 binding to Rab35 is required for its proper localization during cytokinetic abscission. (A) Immunoprecipitation of GFP-FIP1 RBD mutants by mCherry-Rab35. (B) Top: schematic representation of FIP1 constructs used for siFIP1 binucleation rescue experiments, wherein a red asterisk denotes the approximate location of the mutation in the respective construct. Bottom: binucleation percentage of cells either treated with siNT (n=504) or siFIP1 (n=706) coupled with stable expression of rescue constructs containing different domains of FIP1. GFP-FIP1B, n=173; GFP-FIP1B C2, n=189; GFP-FIP1ΔC2, n=98; GFP-FIP1 RBD, n=240; GFP-FIP1ΔRBD, n=136; GFP-FIP1B YS, n=168; GFP-FIP1B IE, n=109; GFP-FIP1B DN, n=160. (C) Top: representative images of two categories of GFP-FIP1B recruitment to the ICB showing either strong or weak/undetected localization, as indicated by the arrowheads. Inverted black and white images of the green channel (FIP1B) are also shown below. Bottom: quantification of the percentage of occurrence for each category in the top panels following either siNT (n=91) or siRab35 (n=135) treatment. Data in B and C are presented as mean±s.e.m. **P<0.01; ***P<0.001; ****P<0.0001; ns, not significant (unpaired two-tailed Student's t-test).

that despite the ability of the individual C2 and RBD domains to bind Rab35 (Fig. 3C), neither domain individually could rescue FIP1 knockdown-induced binucleation (Fig. 4B, lower). The ΔC2 construct also could not rescue the phenotype, suggesting that the middle domain linked to the RBD does not function in cytokinesis (Fig. 4B, lower). Interestingly, the ΔRBD and other RBD mutant constructs that all retain Rab35 binding (Fig. 4A) but lose Rab11b binding (Fig. S3A) displayed the ability to rescue binucleation (Fig. 4B, lower), suggesting that FIP1 function in cytokinesis absolutely requires the C2 domain linked to the middle domain. Of note, as FIP1 seems to act as an atypical effector of Rab35, we sought to determine the impact of the loss of Rab35 on FIP1 localization. We addressed this question using GFP-FIP1B full length in the presence or absence of Rab35. We observed two categories of events, wherein most cells would show strong enrichment of FIP1 to the ICB, whereas the rest showed low to no recruitment of the constructs prior to abscission (Fig. 4C, white arrows). Importantly, we determined that ∼70% of control cells showed strong recruitment of GFP-FIP1B to the ICB prior to abscission (Fig. 4C). However, knockdown of Rab35 significantly shifted this balance towards lesser recruitment, suggesting that Rab35 is important for FIP1 recruitment to the ICB prior to abscission. Our results highlight the importance of FIP1 binding to Rab35 via its C2 domain for its activity in cytokinesis, and strongly suggest that FIP1 function in this process is entirely independent of its classical Rab11 binding.

FIP1 is required for maintaining Rab35 at the midbody

Owing to our results suggesting that FIP1 recruitment may be tied to Rab35, we examined the time delay between their enrichments at both the midbody and the daughter cell-cell interface. By monitoring cells just before (−10 mins) and after telophase (+10 mins) that stably express mCherry-Rab35 or GFP-FIP1B, we demonstrated that, on average, Rab35 tends to enrich at both these locations prior to FIP1 (Fig. 5A). We next examined what happened to Rab35 localization upon the loss of FIP1, as the phenotype of its knockdown is reminiscent of Rab35 knockdown (Kouranti et al., 2006; Dambournet et al., 2011; Frémont et al., 2017; Prekeris, 2011; Klinkert and Echard, 2016). Unexpectedly, during FIP1 knockdown (Fig. 5B), Rab35 levels at the cell-cell interface were significantly lower than in the control (Fig. 5C, bottom left). Most interestingly, Rab35 recruitment to the midbody spiked similarly to the control just after telophase, albeit to a lower absolute level compared to the control, but promptly dropped off ∼1-h post-telophase (Fig. 5C, bottom right). This coincided with the time when FIP1 would have enriched at the midbody (Fig. 5A, right). These results suggest that FIP1 might be required for maintaining Rab35 levels elevated at the midbody to achieve a timely abscission.

FIP1 maintenance of Rab35 and its effectors OCRL and MICAL1 at the midbody is required for curbing actin overaccumulation and cytokinesis defects

Past studies have linked Rab35 activity and its two effectors MICAL1 and OCRL to lowering actin levels at the midbody. Indeed, the absence of either Rab35 or OCRL has been linked to an overaccumulation of actin at the ICB. Thus, we knocked down either FIP1 or Rab35 (Fig. 6A) and verified the ICB actin levels via phalloidin staining. As an endogenous Rab35 antibody that works in immunofluorescence, and could be validated, was not publicly available, we sought to measure the recruitment of its effector MICAL1 instead. Our results clearly demonstrate that actin levels are significantly higher in both FIP1 and Rab35 depletions, whereas MICAL1 recruitment is almost entirely absent in both conditions, suggesting that FIP1 might participate in the ability of Rab35 to recruit its effectors (Fig. 6A). Another Rab35 effector, the phosphatase OCRL, has also been shown to be critical for actin removal prior to abscission (Ben El Kadhi et al., 2012; Dambournet et al., 2011). Indeed, OCRL depletion or mutations that lead to Lowe syndrome have been linked with actin overaccumulation at the ICB, leading to cytokinesis delays. Here, we depleted OCRL and confirmed the induction of cytokinesis delay (Fig. 6B; Fig. S4A). It is of note that in our cell type, OCRL depletion also led to a binucleation phenotype (Fig. 6D). Furthermore, low doses of Latrunculin A (hereafter LatA) treatment have been shown to rescue the phenotype of Rab35 depletion-induced OCRL mislocalization in cell models and in Lowe syndrome patient cells (Dambournet et al., 2011). Strikingly, the same dose of LatA that could rescue the OCRL depletion phenotype of binucleation and cytokinesis delay (Fig. 6B-E; Fig. S4A,B), could also rescue all the phenotypes induced by FIP1 depletion, strongly suggesting that FIP1 is required for maintaining Rab35 levels at the ICB. Finally, as we could observe FIP1 recruitment along the daughter cell-cell interface (Fig. 4C, Fig. 5A), we noted how similar it appears to the recruitment of Rab35 after the first division of Caco-2 cells seeded in three-dimensional cultures (Klinkert and Echard, 2016). In fact, similar to Rab35 depletion, which was reported to induce polarity inversion in Caco-2 cysts, we observed a similar phenotype in FIP1 knockdown (Fig. S4C), again strongly tying FIP1 function to local Rab35 persistence pre-abscission.

DISCUSSION

Our previous studies exploring how Rip11 functions in cytokinesis led us to investigate how class I FIPs might also impact cytokinesis in mammalian cells in a Rab11-independent manner (Laflamme et al., 2017). These results strongly suggest that FIP1 isoforms B and C might retain this evolutionary function in regulating cytokinesis. Importantly, our results suggest that the most critical function of FIP1B and FIP1C in this process is through the linking of their C2 domain to their middle domain. Although, individually, both the C2 and RBD domains become enriched at the ICB, they do not appear to be functional in cytokinesis. Moreover, our results show that the ΔRBD construct can rescue the phenotype, suggesting that other domains in the middle region might also be important but that the C2 domain in the N terminus is critical for FIP function in cytokinesis. Indeed, our results demonstrate that both FIP1B and FIP1C, which contain an N-terminal C2 domain (Fig. 2A) known to bind phosphoinositides (Lindsay and McCaffrey, 2004; Nalefski and

Journal of Cell Science (2021) 134, jcs244384. doi:10.1242/jcs.244384

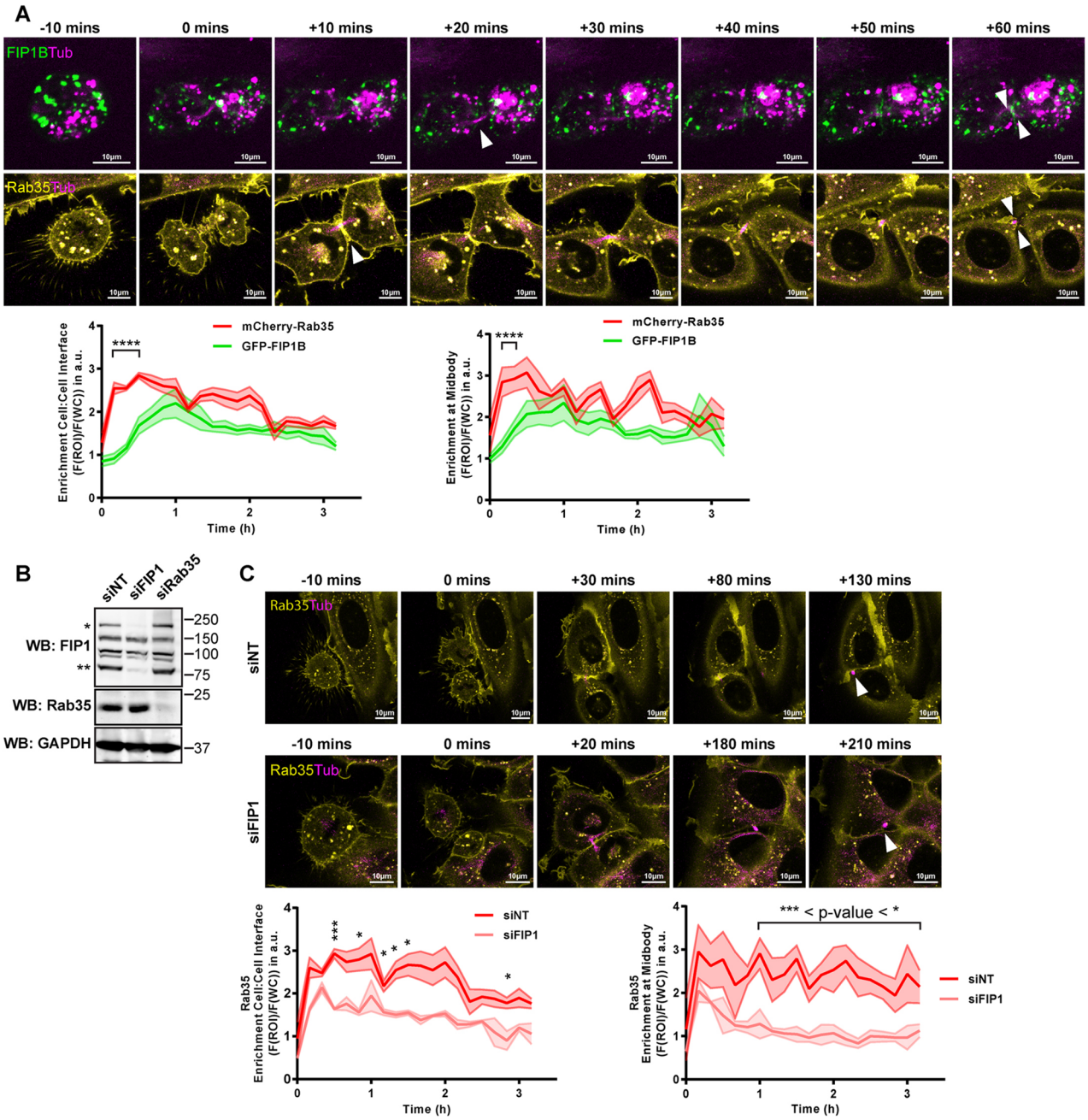

Fig. 5. FIP1 is required for maintaining Rab35 at the midbody. (A) Top: representative images of cells progressing through mitosis that stably express either GFP-FIP1B full length (green) or mCherry-Rab35 (yellow). Cells are stained with SiR-tubulin and tubulin signal is shown in magenta. Time zero is set as the frame corresponding to telophase. Arrowheads denote the ICB linking daughter cells or the remnants of the spindle after abscission. Bottom left: normalized average fluorescence intensity of either GFP-FIP1B (green) or mCherry-Rab35 (red) over time at the cell-cell interface between daughter cells, where time point 0 is the first observance of telophase. mCherry-Rab35, *n*=10; GFP-FIP1B, *n*=18. Bottom right: normalized average fluorescence intensity of either GFP-FIP1B (green) or mCherry-Rab35 (red) over time at the midbody, where time point 0 is the first observance of telophase. mCherry-Rab35, *n*=10; GFP-FIP1B, *n*=18. (B) Representative western blot showing the depletion of FIP1 or Rab35 in the subsequent experiment. FIP1 antibody has non-specific bands and a single asterisk denotes FIP1B, and a double asterisk denotes FIP1C. (C) Top: representative images of cells progressing through mitosis that stably express mCherry-Rab35 (shown in yellow) that were treated with either siNT or siFIP1. Arrowheads denote the location of abscission. Bottom left: normalized average fluorescence intensity of mCherry-Rab35 over time, following either siNT or siFIP1 treatment, at the cell-cell interface between daughter cells, where time point 0 is the first observance of telophase. siNT, *n*=10; siFIP1, *n*=8. Bottom right: normalized average fluorescence intensity of mCherry-Rab35 over time, following either siNT or siFIP1 treatment, at the midbody, where time point 0 is the first observance of telophase. siNT, *n*=10; siFIP1, *n*=8. Data in A and C are presented as mean±s.e.m. **P*<0.05; ****P*<0.001; *****P*<0.0001 (unpaired two-tailed Student's *t*-test). a.u., arbitrary units.

Falke, 1996; Jin and Goldenring, 2006), show dramatically different temporal localizations during mitosis to that of FIP1A (Fig. 2B).

Rab35, one of the proteins identified in the FIP1 Bio-ID (Fig. 3A), has been extensively shown to regulate cytokinesis via the recruitment of major players in the steps prior to abscission (Echard, 2008; Prekeris, 2011; Klinkert and Echard, 2016; Chesneau et al., 2012; Cauvin et al., 2016; Dambournet et al., 2011; Frémont et al., 2017; Kouranti et al., 2006). However, these studies have not

Journal of Cell Science (2021) 134, jcs244384. doi:10.1242/jcs.244384

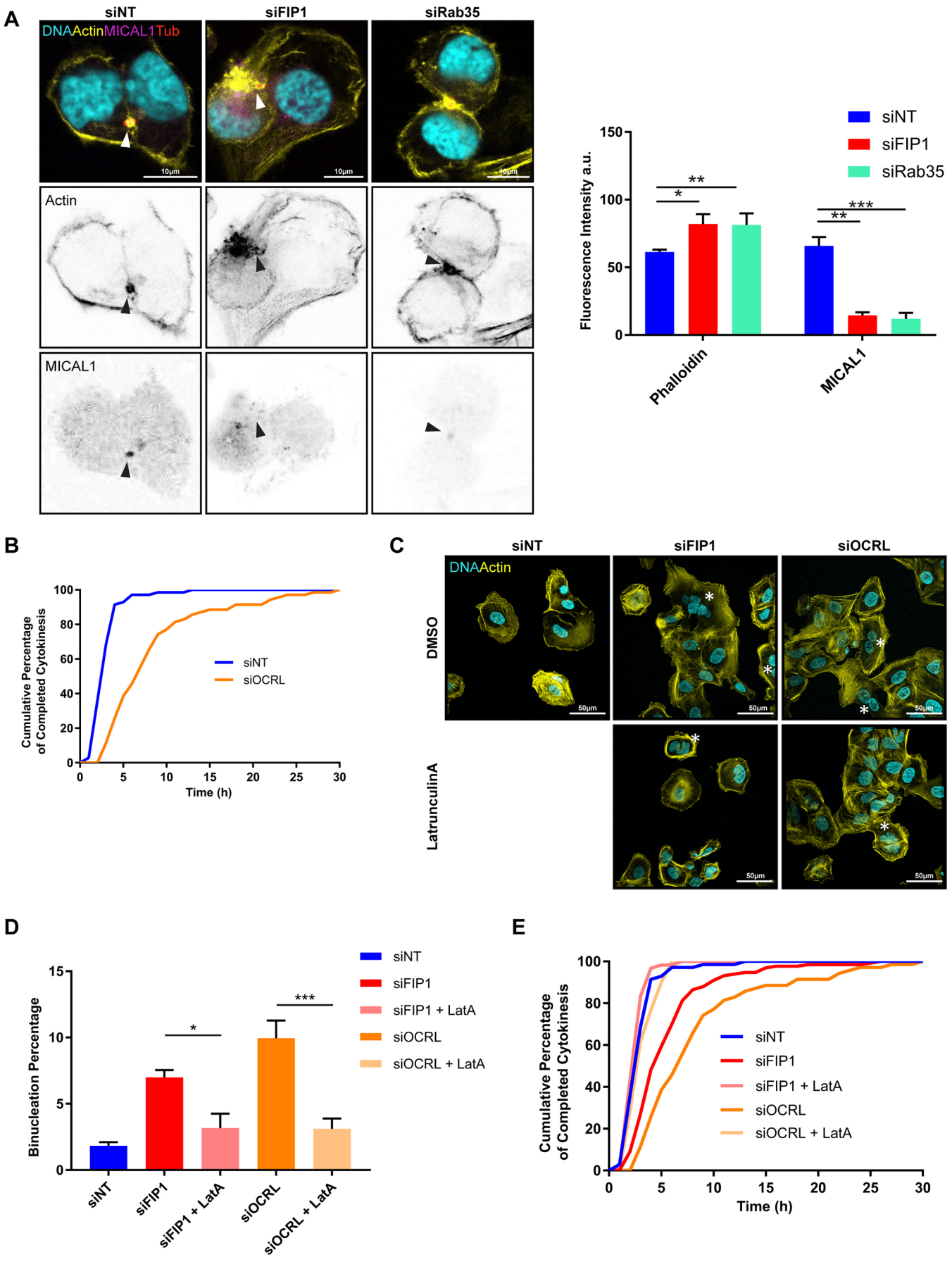

Fig. 6. See next page for legend.

Journal of Cell Science

Journal of Cell Science (2021) 134, jcs244384. doi:10.1242/jcs.244384

Fig. 6. FIP1 maintenance of Rab35 and its effectors OCRL and MICAL1 at the midbody is required for curbing actin overaccumulation and cytokinesis defects. (A) Left: representative images of cells treated with either siNT, siFIP1 or siRab35, wherein DNA is stained in cyan, actin in yellow, MICAL1 in magenta and β-tubulin in red. Inverted black and white images of the yellow channel of actin and magenta channel of MICAL1 are shown below. Arrowheads indicate either the accumulation of actin at the ICB or the localization of MICAL1 in the midbody. Right: quantification of either actin or MICAL1 average normalized fluorescence intensity signal in an ROI around the ICB, measured as the region of β-tubulin staining and surrounding area in siNT (n=12), siFIP1 (n=11) or siRab35 (n=13) conditions. Fluorescence intensity was measured as the fluorescence intensity minus that of the background signal. (B) Cumulative percentage of cells depleted of OCRL having completed cytokinesis. (C) Representative immunofluorescence of cells treated with either siNT, siFIP1 or siOCRL, followed by treatment with either DMSO or LatA. Binucleated cells are indicated with white asterisks. (D) Binucleation percentage of cells treated with siNT (n=504), siFIP1 (n=766) or OCRL (n=522), and subsequently treated with LatA (siFIP1, n=300; siOCRL, n=300) as indicated in Materials and Methods. (E) Cumulative cytokinesis timing for siNT (n=70), siFIP1 (n=133) and siOCRL (n=70) either treated with or without LatA (siFIP1, n=60; siOCRL, n=61) over time. Data in A and D are presented as mean±s.e.m. *P<0.05, **P<0.01, ***P<0.001 (unpaired two-tailed Student's t-test). a.u., arbitrary units.

explored the means by which Rab35 is recruited to the ICB during this process. Here, our data show that Rab35 is tethered to the ICB by binding FIP1, as its recruitment occurs prior to that of FIP1 (Fig. 5B). In other words, FIP1 presence seems to be important for maintaining Rab35 levels at the ICB, as its depletion causes a dramatic drop off of Rab35 in the minutes following its recruitment (Fig. 5C). We believe this leads to the overaccumulation of actin and subsequent cytokinesis delays that we observed.

In fact, one of the few studies that did explore Rab35 recruitment during mitosis identified that Rab35 regulates apicobasal polarity by regulating apical membrane initiation site (AMIS) formation in Caco-2 cysts, wherein its depletion induces apical component mislocalization and polarity inversion (Klinkert et al., 2016). However, this was linked to direct binding between Rab35 and PODXL at the apical membrane, thus tethering Rab35 to this location. Our results suggest that FIP1 depletion also induces a similar polarity inversion in this cell type, to a similar degree to the depletion of Rab35. It would be interesting to investigate how FIP1 functions in the Rab35:PODXL axis. Indeed, although our data suggest that FIP1 tethers Rab35 to the ICB, the recruitment of Rab35 per se was recently shown to be mediated by IRSp53, which regulates the Rab35:PODXL axis during lumen formation by binding and recruiting Rab35S22N to the AMIS (Bisi et al., 2020). Whether FIP1 participates in this process directly or in parallel will need further study. On a side note, our results in this cell type do not seem to concur with previous research suggesting that FIP5 is important for AMIS formation in a Rab11-dependent manner in MDCK cells, as our results do not indicate that FIP5 has any impact on AMIS formation in Caco-2 cells; however, this could be attributed to differences in cell lines and/or lack of complete depletion due to siRNA-mediated knockdowns of proteins in our experiments (Li et al., 2014b; Willenborg et al., 2011).

More specifically, our structure function and biochemical analysis revealed that FIP1 isoforms demonstrate a preference for the dominant-negative form of Rab35 (Fig. 3D-E; Fig. S2D), suggesting that they may be atypical effectors similar to IRSp53. This raises an interesting question that our data does address however, and that is how 'inactive' Rab35, bound to GDP, recruited by IRSp53 and maintained by FIP1, might then be activated to then recruit its downstream effectors, such as MICAL1 and OCRL, to regulate actin levels in the ICB.

Furthermore, although we could detect binding between either the C2 domain or the RBD domain of FIP1 with Rab35 in cells, we could only confirm direct binding between Rab35:RBD using *in vitro* experiments, which suggests that either the C2 domain binding is indirect, or that the binding requires something not recapitulated by our *in vitro* system, such as, for example, a cellular or lipidic environment or post-translational modifications. This would require further study into the precise function of the FIP1 C2 domain in this context. One such function could be that FIP1 tethers together different vesicles, in a similar manner to the Rab5 effector Rabenosyn-5, which links $Rab4^+$ and $Rab5^+$ vesicles (de Renzis et al., 2002). Our results indicate that in cells, FIP1 can possibly bind Rab35 with its C2 domain and bind to several different Rabs, including Rab11, Rab14 and Rab35 with its RBD. It is possible that tethering Rab35 to Rab11 vesicles may have a function in other cellular contexts, similar to the function of Rabenosyn-5. However, as we could not observe any Rab11 in our Rab35 pulldowns (Fig. 3D), this might only occur for discrete short-lived interactions. These interactions would most likely be dispensable for FIP1 cytokinetic function, as our results clearly indicate that the RBD of FIP1 is dispensable for this function. In other words, FIP1 function in cytokinesis is Rab11-independent, similar to what we observed for Rip11 (Laflamme et al., 2017).

Importantly, our results indicate that the C2 domain can dimerize with full-length FIP1 (Fig. S2B). This could be the means by which FIP1 maintains Rab35 at the ICB. Indeed, in this case, FIP1 might act as a scaffold rather than a traditional effector per se. Furthermore, this does not exclude the possibility that the FIP1 C2 domain might homodimerize or heterodimerize with other FIP C2 domains, such as that of FIP2 or FIP5. These interactions might be important for specific cellular functions, but as neither FIP2 nor FIP5 depletion induced a cytokinesis phenotype, this was not pursued.

In conclusion, this work has led to the identification of a new function for class I FIPs in cytokinesis, and that this function is independent of Rab11 binding. We have also shown that this function is implicated in the Rab35:OCRL:MICAL1 axis involved in regulating actin levels at the ICB prior to abscission in both two-dimensional and three-dimensional cultures (Fig. S4D). These results will be an important stepping stone for further study into the various mechanisms that lead to abscission, and this will have far reaching implications as cell division regulates virtually all cellular processes.

MATERIALS AND METHODS

Cell culture and transfections

U2OS, HEK293T, HCT116, HeLa, A375, A549 and MCF7 cells were maintained in 5% CO_2 and at 37°C in Dulbecco's modified Eagle's medium (DMEM, Life Technologies Gibco) supplemented with 10% fetal bovine serum (Wisent), 100 µg/ml Streptomycin (Life Technologies) and 100 U/ml of Penicillin (Life Technologies). Transfex (ATCC) was used following the manufacturer's instructions for transfecting U2OS cells for exogenous expression, whereas polyethylenimine (Polysciences, 23966-1) was used to transfect HEK293T cells for immunoprecipitation experiments. Cells were routinely verified for mycoplasma contamination. As for stable cells lines, U2OS cells were transfected with exogenous constructs and selected using 100 µg/ml of hygromycin B or 700 µg/ml of G418, depending on the backbone resistance of the plasmid. Resistant cells were sorted using FACS analysis, 7 days post selection, to produce a heterogeneous population of cells expressing low to medium expression of the different constructs. Cells were then maintained in selection medium for at least 14 days prior to any experiment being performed to ensure stable integration of the constructs into the genome. For LatA treatment, following 72 h of protein depletion by siRNA, cells were plated for immunofluorescence similarly to other experiments, but 8 nM of LatA was added into the media. Cells were fixed

24 h after plating and cell binucleation was assayed similarly to other experiments.

Plasmids

pCDNA3.1-pEGFP-C1-Rab11FIP1A, pCDNA3.1-pEGFP-C1-Rab11FIP1B and pCDNA3.1-pEGFP-C1-Rab11FIP1C were gracious gifts from James Goldenring, Vanderbilt University Medical Center, TN, USA. pCDNA3.1-pEGFP-C1-empty was produced by removing the Rab11FIP1 insert by PCR linearization of the pCDNA3.1-pEGFP-C1-Rab11FIP1B plasmid and then closing the plasmid by using a KLD enzyme kit (New England Biolabs, M0554) following the manufacturer's instructions. The pCDNA3.1-mCherry-Rab35 plasmid was produced by first amplifying Rab35 from a U2OS cDNA preparation using the following two primers: 5′-ATCGGGTACCATGGCCCGGGACTACGACCAC-3′ and 5′-ATCGTCTAGATTAGCAGCAGCGTTTCTTTCG-3′. Rab35 was then cloned into the pCDNA3.1-mCherry-empty vector (a gracious gift from Marc Therrien, IRIC, Université de Montréal, QC, Canada) using KpnI and XbaI restriction enzyme sites. The N-terminal deletion constructs of Rab11FIP1 were produced using the Q5 polymerase (New England Biolabs, M0491) deletion strategy coupled to a KLD reaction kit for the closing of the plasmid. Specifically, the primer 5′-GGTGACGATAA-CAAGGGCG-3′ was used in conjunction with either 5′-CAGCTCTCC-GAATCTTCC-3′ (to produce 380-1283), 5′-GATTCTCTGATGGGCAGG-3′ (to produce 669-1283), 5′-ACTCAGTATCAGAGCAAAG-3′ (to produce 920-1283), 5′-AGACTTCATCCTGTGAAG-3′ (to produce 1175-1283) or 5′-AAGAAATACAGCCCCTCG-3′ (to produce 1211-1283). As for deletion constructs 1-208, primer pair 5′-TAAAAGGGCGAATTCTGC-3′ was used with 5′-AACCACAGACTCATCATC-3′ and the plasmid was again closed using a KLD enzyme kit. As for deletion construct 108-1211, primers 5′-GGTGACGATAACAAGGGCG-3′ and 5′-GAGGTGGACCTGCGGGAT-3′ were used to produce 108-1283. This plasmid was then used with primers 5′-CATCATGACCTCATTGTTCAAGTTC-3′ and 5′-TAAAAGGGCGAA-TTCTGC-3′ to produce 108-1211. Again, linear plasmid was closed using a KLD enzyme kit. For deletion construct 1-1211, the same primer set used to produce 108-1211 was used on the full-length Rab11FIP1B plasmid. Finally, the three mutant constructs Y1254S, I1255E and D1256N were produced using the following primer pairs, respectively: 5′-GCTGGAAGACtccATT-GACAACCTGC-3′ and 5′-TCGCGGACCTGGAACTCC-3′; 5′-GGAA-GACTACgaaGACAACCTGCTTGTCAGGGTC-3′ and 5′-AGCTCGCG-GACCTGGAAC-3′; and 5′-AGACTACATTaacAACCTGCTTGTCAGGG-3′ and 5′-TCCAGCTCGCGGACCTGG-3′. The lowercase letters in the three previous primer pairs denote the mutated nucleotides with which the construct mutations were created. For mApple constructs, mApple-Farnesyl-5 was obtained as a gift from Michael Davidson (Addgene plasmid, 54899; RRID:Addgene_54899). This plasmid was first linearized using the primer pair 5′-AATTCTGCAGTCGACGGTACC-3′ and 5′-CGAAGCTTGAGCTCGAGATC-3′. Next the three FIPs, FIP1A, FIP1B and FIP1C were respectively amplified using the primer pairs 5′-gatctc-gagctcaagcttcgATGGGCAGGACCCGTGAG-3′ and 5′-gtaccg-tcgactgcagaattTTACATCTTTCCTGCTTTTTTGCCAAC-3′ (FIP1A); 5′-gatctcgagctcaagcttcgATGTCCCTAATGGTCTCG-3′ and 5′-gtaccgtc-gactgcagaattTTACATCTTTCCTGCTTTTTTG-3′ (FIP1B); and 5′-gat-ctcgagctcaagcttcgATGTCCCTAATGGTCTCG-3′ and 5′-gtaccgtcgac-tgcagaattTTACATCTTTCCTGCTTTTTTG-3′ (FIP1C). These fragments, along with the linearized mApple plasmid, were assembled using Gibson assembly (New England Biolabs, E2611), following the manufacturer's instructions. For bacterial plasmids, pET28a and pGEX-6p1 were obtained from the Benjamin Kwok lab, IRIC, Université de Montréal, QC, Canada, and digested with EcoRI/XhoI to linearize them. Then, Rab11FIP1B C2 domain and RBD domain were amplified using the respective primers 5′-ATCGGAATTCATGTCCCTAATGGTCTCG-3′ and 5′-ATCGCTC-GAGTAAACCACAGACTCATCA-3′ (C2 domain), and 5′-ATCG-GAATTCAAGAAATACAGCCCCTCG-3′ and 5′-ATCGCTCGAGTTA-CATCTTTCCTGCTTT-3′ (RBD domain). These two fragments were digested with EcoRI/XhoI and assembled into the pET28a plasmid using a standard ligation protocol. Rab35WT was amplified using the primers 5′-ATCGGAATTCATGGCCCGGGACTACGAC-3′ and 5′-ATCGCTCGA-GTTAGCAGCAGCGTTTCTT-3′. This was then digested with EcoRI/XhoI and assembled into pGEX-6P1. p-DEST15(GST)-Rab11A was a gracious gift from the Matt Smith lab, IRIC, Université de Montréal, QC, Canada. EGFP-Rab1A (Addgene, 49467; RRID, Addgene_49467), EGFP-Rab5 (Addgene, 49888; RRID, Addgene_49888), EGFP-Rab6A (Addgene, 49469; RRID, Addgene_49469), EGFP-Rab13 (Addgene, 49548; RRID, Addgene_49548) and EGFP-Rab35 (Addgene, 49552; RRID, Addgene_49552) were gifts from Marci Scidmore. GFP-RAB10 was a gift from Michael Bassik (Addgene, 130883; RRID, Addgene_130883). GFP-Rab11 WT was a gift from Richard Pagano (Addgene, 12674; RRID, Addgene_12674). All constructs were validated by sequencing.

Antibodies and other staining reagents

Primary antibodies used were as follows: Rab11FIP1 (Sigma-Aldrich, HPA025960, used at 1/1000); Rab11FIP2 (Sigma-Aldrich, HPA037726, used at 1/1000); Rab11FIP5 (Sigma-Aldrich, HPA036407, used at 1/1000); Rab11FIP3 (Proteintech, 25843-1-AP, used at 1/100 for immunofluorescence); actin [Millipore (C4), MAB1501, used at 1/10,000]; GFP [Santa Cruz Biotechnology (B-2), sc-9996, used at 1/2000]; GAPDH [Santa Cruz Biotechnology (FL-335), sc-25778, used at 1/1000]; mCherry for immunoprecipitation (Abcam, ab183628, 1 µg used per immunoprecipitation condition); mCherry for western blotting (Abcam, ab167453, used at 1/2000); MICAL1 (Proteintech, 14818-1-AP, used at 1/100 for immunofluorescence); Rab35 (Proteintech, 11329-2-AP, used at 1/1000); MKLP1 (Abcam, ab168964, used at 1/100 for immunofluorescence); CHMP4B (Proteintech, 13683-1-AP, used at 1/100 for immunofluorescence); His-probe [Santa Cruz Biotechnology (H-15), sc-803, used at 1/1000]; β-Tubulin (Abcam, ab6046, used at 1/2000); and α-Tubulin [Cell Signaling Technology (DM1A), 3873, used at 1/1000 for immunofluorescence]. Secondary antibodies used for western blotting and immunoprecipitation were AffiniPur goat anti-rabbit (H+L) (Jackson Immunoresearch, 111-035-144, used at 1/1000), AffiniPur mouse anti-rabbit (light chain specific) (Jackson Immunoresearch, 211-032-171, used at 1/1000), AffiniPur goat anti-mouse (light chain specific) (Jackson Immunoresearch, 115-035-174, used at 1/1000) and AffiniPur goat anti-mouse (H+L) (Jackson Immunoresearch, 115-035-062, used at 1/1000). Secondary antibodies and other reagents used for immunofluorescence were Alexa Fluor 488 phalloidin (Invitrogen, A12379, used at 1/1000), Alexa Fluor 555 phalloidin (Invitrogen, A34055, used at 1/1000), Alexa Fluor 647 phalloidin (Invitrogen, A22287, used at 1/50), Alexa Fluor 488 goat anti-mouse IgG (Invitrogen, A11029, used at 1/1000), Alexa Fluor 488 goat anti-rabbit IgG (Invitrogen, A11008, used at 1/1000), Alexa Fluor 555 anti-mouse IgG (Cell Signaling Technology, 4499S, used at 1/1000), Alexa Fluor 555 anti-rabbit IgG (Cell Signaling Technology, 4413S, used at 1/1000), Alexa Fluor 633 goat anti-rabbit IgG (Invitrogen, A31577, used at 1/1000) and Alexa Fluor 635 goat anti-mouse IgG (Invitrogen, A31575, used at 1/1000), DAPI was used to stain nuclei at 1 µg/ml. SiR-Tubulin (Cytoskeleton, Inc., CY-SC002, used at 100 nM) was used to monitor tubulin polymerization during live-cell imaging.

siRNA treatments

Lipofectamine RNAiMax (Thermo Fisher Scientific, 13778100) was used to transfect cells using siRNA. RNAi duplex sequences used for siRNA were as follows: siControl, 5′-UUCUCCGAACGUGUCACGUdTdT-3′ and 5′-ACGUGACACGUUCGGAGAAdTdT-3′; siFIP1, 5′-UUAAUU-GUAAUCAUUAACCdTdG-3′ and 5′-GGUUAAUGAUUACAAUUAA-dTdT-3′; Rab35, 5′-GCUCACGAAGAACAGUAAA-3′ and 5′-UUUA-CUGUUCUUCGUGAGC-3′. siRNA sequences against FIP2, FIP5 and OCRL were obtained from Qiagen, wherein sequences are proprietary and unknown. Targeted sequences were as follows: siFIP2 5′-CAGGTGG-CAATCAATCTCAAT-3′; siFIP5 5′-CACCATCCAGTTCACGCGCAA-3′; and siOCRL 5′-CAGCGGGAGGGTCTCATCAAA-3′.

Western blotting and immunoprecipitation

For western blotting, cells were scraped in 50 mM Tris (pH 7.5) containing 1% SDS, sonicated at 70% intensity for 1 min and then boiled for 5 min at 95°C. Samples were then quantified using a BCA Protein Assay Kit (Thermo Scientific, Pierce, 23225). Samples were then mixed with 5× SDS sample loading buffer and loaded onto SDS-PAGE gels (7-15%) to separate

proteins according to their molecular weight. Proteins were then transferred onto nitrocellulose and blotted using the indicated antibodies following standard laboratory procedures. As for immunoprecipitations, cells were scraped in PBS and spun down to form a pellet. Pellets were kept at −80°C until used. Pellets were then lysed in lysis buffer containing 50 mM Tris (pH 7.5), 5 mM EDTA, 1% Triton X-100 and 150 mM NaCl supplemented with protease inhibitor cocktail (Roche cOmplete, 11697498001), 2 mM imidazole (BioShop, IMD508), 1 mM sodium fluoride (Sigma-Aldrich, S6776), 6 mM sodium molybdate (Sigma-Aldrich (M1651), 10 mM sodium tartrate (Sigma-Aldrich, S4797), 1.2 mM β-glycerophosphate (Sigma-Aldrich, G5422), 1 mM sodium orthovanadate (Sigma-Aldrich, S6508) and 100 nM sodium pyrophosphate (Sigma-Aldrich, 221368) to inhibit all proteases and phosphatases. Lysis occurred for 15 min on ice before samples were spun down at 21,000 ***g*** for 15 min. Supernatants were then quantified using the Bradford Reagent (Bio-Rad Protein Assay Dye, 5000006). Next, between 1-2 mg of total protein from each sample was incubated overnight with 1 µg of primary antibody and pre-blocked Protein A/G-PLUS Agarose beads (Santa Cruz Biotechnology, sc-2003). The following morning, the beads were washed five times using lysis buffer and then SDS sample buffer was added followed by boiling to detach proteins from the beads. Immunoprecipitated samples were then loaded on SDS-PAGE gels similar to above.

Immunofluorescence

Cells plated for immunofluorescence were left to adhere onto coverslips overnight and fixed using 4% paraformaldehyde (PFA). Slides were then washed twice using immunofluorescence wash buffer composed of PBS supplemented with 0.1% Triton X-100. Slides were then incubated for 1 h at room temperature in immunofluorescence blocking buffer composed of PBS, 0.3% Triton X-100 and 5% bovine serum albumin (BSA) passed through a 0.22 µm filter. Next, the slides were incubated in primary antibodies overnight, all of which were mixed in immunofluoresence blocking buffer. Slides were then washed three times for 5 min each using immunofluorescence wash buffer, and then incubated with secondary antibodies for 2 h at room temperature. Finally, slides were again washed three times for 5 min each, before being mounted in Vectashield (Vector Laboratories Canada, H-1000) and sealed using nail polish. Immunofluorescence was observed using an inverted confocal LSM880 microscope from Zeiss using either a 20× Plan Apo, NA 0.8, DICII objective for binucleation measurements, a 40× EC PlnN, NA 1.3, DIC III objective for phalloidin staining and MICAL1 enrichment measurements, or a 63× Plan-Apo, NA 1.4 DIC objective for MKLP1, RhoA, FIP3 and CHMP4B recruitment.

GST-pulldown assay

Bacterial protein production

DH5α bacteria containing plasmids coding for His-C2, His-RBD, GST-, GST-Rab11 and GST-Rab35 WT were inoculated into 50 ml culture with antibiotics overnight. The following morning, the 50 ml cultures were diluted into 500 ml cultures containing antibiotics and 1 mM of isopropyl-β-D-thiogalactoside (BioShop, IPT001) for 8 h. Cultures were then spun down to pellets and two different lysis were performed. For His-tagged proteins, bacteria were lysed for 15 min on ice in Ni-NTA Lysis buffer composed of 50 mM NaH_2PO_4 (BioShop, SPM306), 300 mM NaCl and 10 mM imidazole (BioShop, IMD508) (pH 8.0). Next, 1 mg/ml of lysozome (BioShop, LYS702) was added to the lysis for another 30 min on ice. Samples were then sonicated for six 10 s bursts at 100% intensity, allowing for 10 s of cooling period between each burst. Samples were then centrifuged at 3000 ***g*** for 1 h at 4°C to pellet debris, and the supernatant was then filtered through a 0.44 µm filter. Supernatants were then incubated with 1 ml of Ni-NTA resin (Qiagen, 1018244) overnight at 4°C. The following day, beads were washed with Ni-NTA wash buffer, composed of Ni-NTA lysis buffer but containing 20 mM of imidazole (BioShop, IMD508), a total of five times with 5 ml of wash buffer. Proteins were then eluted using Ni-NTA elution buffer composed of Ni-NTA lysis buffer but containing 250 mM imidazole. The elutions were kept at −80°C until needed. For the GST protein production, bacterial pellets were resuspended in GST Lysis buffer containing 1 mM dithiothreitol (DTT), 1 mM phenylmethylsulfonyl fluoride, 1 mM EDTA and 0.2% Triton X-100 in PBS (pH 7.5). To this, 1 mg/ml of lysozyme (BioShop, LYS702) was added followed by vigorous shaking, and the samples were left on ice for 60 min with occasional shaking. Samples were sonicated similarly to His-tagged proteins. Samples were then centrifuged at 3000 ***g*** for 1 h at 4°C, and supernatants were then filtered through a 0.44 µm filter. Samples were then rotated overnight at 4°C with 1 ml of gluthathione resin (GenScript, L00206). The following morning, beads were washed five times with PBS and beads were kept as a 20% slurry at 4°C until needed.

In vitro nucleotide loading

Guanosine 5′-[β,γ-imido]triphosphate (Sigma-Aldrich, G0635) and Guanosine 5′-[β-thio]diphosphate (Sigma-Aldrich, G7637) 100× solutions (20 mM and 100 mM, respectively) were prepared in distilled water. 1× solutions were then incubated with 5 µg of GST-Rab11 or GST-Rab35 beads for 1 h at 37°C in loading buffer composed of 25 mM Tris (pH 7.5), 100 mM NaCl, 10 mM EDTA, 5 mM $MgCl_2$ and 1 mM DTT. The loading reaction was then halted by the addition of 20 mM $MgCl_2$.

GST-pulldown assay

Either purified proteins (for His-tags) or beads (GST-proteins) were loaded on SDS-PAGE gels beside a BSA ladder to quantify samples. Using these measurements, 5 µg of His-C2 or His-RBD were incubated overnight at 4°C with 5 µg of either GST-, GST-Rab11 or GST-Rab35 (either empty, loaded with GTP or loaded with GDP and completed to the same bead bed using empty glutathione agarose beads) in IVB buffer composed of 50 mM Tris (pH 7.5), 100 mM NaCl, 10 mM $MgCl_2$, 0.1% Triton X-100 and 0.05% BSA. The following day, beads were washed five times with IVB buffer and then proteins were eluted using SDS sample loading buffer. Proteins were then loaded on SDS-PAGE gels and proteins were revealed using Coomassie Brilliant Blue Staining.

Three-dimensional cultures

For three-dimensional cultures, a thin layer of GelTrex (Gibco, A14132-02) was spread out into the bottom of an Ibidi eight-well chamber slide (Ibidi, 80826) and left to solidify in the cell culture incubator at 5% CO_2 and 37°C for 15 min. Next, cells were trypsinized and 10,000 cells of an individualized cell solution in DMEM supplemented with 2% GelTrex were layered on the solidified basal layer. Medium was delicately removed and changed every 3 days for a total of 10 days before cells were fixed using 4% PFA, and whole wells were treated for immunofluorescence similarly to cells on slides.

Live imaging

Cells plated for live imaging were first counted, and 10,000 cells were plated similarly to other cell lines explained above into Ibidi eight-well chamber slides in the presence of 100 nmol of SiR-Tubulin (Cytoskeleton, Inc., CY-SC002) for 24 h prior to imaging to avoid altering microtubule dynamics. Slides were then mounted into an LSM700 live-cell imaging mount on an inverted LSM700 confocal microscope (Zeiss) to maintain 5% CO_2 and 37°C during movie acquisitions. Cells were filmed using either a 20× Plan Apo, NA 0.8, DICII objective or a 40× Plan Apo, NA 1.4 DIC objective, and movies were acquired using Zen software.

Fluorescence intensity measurements

For fluorescence intensity measurements, individual frames of live-imaging movies were first sequentially opened in ImageJ as a stacked image. Next, for different measurements, the custom region function was used to draw a custom region of interest (ROI), which either followed the cell-cell interface or the entire SiR-tubulin-stained mitotic spindle in the far-red channel. These regions were then measured for average fluorescence signal in the appropriate green and red channels, and a measurement of the average fluorescence intensity of the entire cell was also used to normalize the enrichment signals. This was then repeated for every time point over the course of the movie and graphs of the averages were produced using GraphPad Prism software. Dark lines represent the average signal, whereas

the shaded areas represent the s.e.m. over time. A two-tailed Student's *t*-test was then used for each point to compare significance.

Statistical analyses

Paired and unpaired two-tailed Student's *t*-tests and Mann–Whitney tests were performed using the GraphPad Prism. Values are expressed as mean±s.e.m. or mean±s.d., as indicated in the figure legends. *P*-values are noted on the figures, wherein **P*<0.05, ***P*<0.01, ****P*<0.001, *****P*<0.0001. Tests were carried out on at least three independent experiments and then all individual points were pooled together to produce figures, unless the data specifically show means.

Acknowledgements

We thank Giorgio Scita (University of Milan, Italy) for his input on the manuscript; the Goldenring lab (Vanderbilt University Medical Center, TN, USA) for the pEGFP-FIP1A, pEGFP-FIP1B and pEGFP-FIP1C plasmids; the Smith lab (IRIC, Université de Montréal, Canada) for the p-DEST15(GST)-Rab11A plasmid; the Echard lab (Institut Pasteur, Paris, France) for the siRNA targeting Rab35; the Piekny lab (University of Concordia, Montreal, Canada) for the pEGFP-RhoA-binding-domain-of-anillin plasmid; the Therrien lab (IRIC, Université de Montréal) for the pCDNA3.1-mCherry-empty plasmid, as well as the 293T, HCT116, A375, A549, MCF7 and Caco-2 cell lines; the Borden lab (IRIC, Université de Montréal) for the U2OS cell line; and the Meloche lab (IRIC Université de Montréal) for the HeLa cell line. We also thank Christian Charbonneau from the core microscopy platform (IRIC, Université de Montréal) for assistance in all microscopy experiments, as well as the fluorescence-activated cell sorting (FACS) platform (IRIC, Université de Montréal) for the FACS experiments.

Competing interests

The authors declare no competing or financial interests.

Author contributions

Conceptualization: N.V.G.I., G.E.; Methodology: N.V.G.I.; Investigation: N.V.G.I.; Writing - original draft: N.V.G.I.; Writing - review & editing: N.V.G.I., G.E.; Supervision: G.E.; Project administration: G.E.; Funding acquisition: N.V.G.I., G.E.

Funding

This work was supported by the Canadian Institutes of Health Research operating grant (MOP-148560) and a discovery grant from the Natural Sciences and Engineering Research Council of Canada. N.V.G.I. received an Institut de Recherche en Immunologie et en Cancérologie PhD scholarship, as well as a PhD funding scholarship from Fonds de Recherche du Québec - Nature et Technologies.

References

Ai, E. and Skop, A. R. (2009). Endosomal recycling regulation during cytokinesis. *Commun. Integr. Biol.* **2**, 444-447. doi:10.4161/cib.2.5.8931

Baetz, N. W. and Goldenring, J. R. (2013). Rab11-family interacting proteins define spatially and temporally distinct regions within the dynamic Rab11a-dependent recycling system. *Mol. Biol. Cell* **24**, 643-658. doi:10.1091/mbc.e12-09-0659

Ben El Kadhi, K., Emery, G. and Carreno, S. (2012). The unexpected role of Drosophila OCRL during cytokinesis. *Commun. Integr. Biol.* **5**, 291-293. doi:10.4161/cib.19914

Bisi, S., Marchesi, S., Rizvi, A., Carra, D., Beznoussenko, G. V., Ferrara, I., Deflorian, G., Mironov, A., Bertalot, G., Pisati, F. et al. (2020). IRSp53 controls plasma membrane shape and polarized transport at the nascent lumen in epithelial tubules. *Nat. Commun.* **11**, 3516. doi:10.1038/s41467-020-17091-x

Bökenkamp, A. and Ludwig, M. (2016). The oculocerebrorenal syndrome of Lowe: an update. *Pediatr. Nephrol.* **31**, 2201-2212. doi:10.1007/s00467-016-3343-3

Bruno, J., Brumfield, A., Chaudhary, N., Iaea, D. and Mcgraw, T. E. (2016). SEC16A is a RAB10 effector required for insulin-stimulated GLUT4 trafficking in adipocytes. *J. Cell Biol.* **214**, 61-76. doi:10.1083/jcb.201509052

Carim, S. C., Ben El Kadhi, K., Yan, G., Sweeney, S. T., Hickson, G. R., Carréno, S. and Lowe, M. (2019). IPIP27 coordinates PtdIns(4,5)P2 homeostasis for successful cytokinesis. *Curr. Biol.* **29**, 775-789.e7. doi:10.1016/j.cub.2019.01.043

Carson, B. P., Del Bas, J. M., Moreno-Navarrete, J. M., Fernandez-Real, J. M. and Mora, S. (2013). The rab11 effector protein FIP1 regulates adiponectin trafficking and secretion. *PLoS ONE* **8**, e74687. doi:10.1371/journal.pone.0074687

Cauvin, C., Rosendale, M., Gupta-Rossi, N., Rocancourt, M., Larraufie, P., Salomon, R., Perrais, D. and Echard, A. (2016). Rab35 GTPase triggers switch-like recruitment of the lowe syndrome lipid phosphatase OCRL on newborn endosomes. *Curr. Biol.* **26**, 120-128. doi:10.1016/j.cub.2015.11.040

Chesneau, L., Dambournet, D., Machicoane, M., Kouranti, I., Fukuda, M., Goud, B. and Echard, A. (2012). An ARF6/Rab35 GTPase cascade for endocytic recycling and successful cytokinesis. *Curr. Biol.* **22**, 147-153. doi:10.1016/j.cub.2011.11.058

Dambournet, D., Machicoane, M., Chesneau, L., Sachse, M., Rocancourt, M., El Marjou, A., Formstecher, E., Salomon, R., Goud, B. and Echard, A. (2011). Rab35 GTPase and OCRL phosphatase remodel lipids and F-actin for successful cytokinesis. *Nat. Cell Biol.* **13**, 981-988. doi:10.1038/ncb2279

De Renzis, S., Sönnichsen, B. and Zerial, M. (2002). Divalent Rab effectors regulate the sub-compartmental organization and sorting of early endosomes. *Nat. Cell Biol.* **4**, 124-133. doi:10.1038/ncb744

Echard, A. (2008). Membrane traffic and polarization of lipid domains during cytokinesis. *Biochem. Soc. Trans.* **36**, 395-399. doi:10.1042/BST0360395

Erneux, C., Ghosh, S., Ramos, A. R. and Edimo, W. E. (2016). New functions of the inositol polyphosphate 5-phosphatases in cancer. *Curr. Pharm. Des.* **22**, 2309-2314. doi:10.2174/1381612822666160226132512

Eva, R., Dassie, E., Caswell, P. T., Dick, G., Ffrench-Constant, C., Norman, J. C. and Fawcett, J. W. (2010). Rab11 and its effector Rab coupling protein contribute to the trafficking of beta 1 integrins during axon growth in adult dorsal root ganglion neurons and PC12 cells. *J. Neurosci.* **30**, 11654-11669. doi:10.1523/JNEUROSCI.2425-10.2010

Fan, G.-H., Lapierre, L. A., Goldenring, J. R. and Richmond, A. (2003). Differential regulation of CXCR2 trafficking by Rab GTPases. *Blood* **101**, 2115-2124. doi:10.1182/blood-2002-07-1965

Fan, G.-H., Lapierre, L. A., Goldenring, J. R., Sai, J. and Richmond, A. (2004). Rab11-family interacting protein 2 and myosin Vb are required for CXCR2 recycling and receptor-mediated chemotaxis. *Mol. Biol. Cell* **15**, 2456-2469. doi:10.1091/mbc.e03-09-0706

Festa, B. P., Berquez, M., Gassama, A., Amrein, I., Ismail, H. M., Samardzija, M., Staiano, L., Luciani, A., Grimm, C., Nussbaum, R. L. et al. (2019). OCRL deficiency impairs endolysosomal function in a humanized mouse model for Lowe syndrome and Dent disease. *Hum. Mol. Genet.* **28**, 1931-1946. doi:10.1093/hmg/ddy449

Frémont, S. and Echard, A. (2018). Membrane traffic in the late steps of cytokinesis. *Curr. Biol.* **28**, R458-R470. doi:10.1016/j.cub.2018.01.019

Frémont, S., Hammich, H., Bai, J., Wioland, H., Klinkert, K., Rocancourt, M., Kikuti, C., Stroebel, D., Romet-Lemonne, G., Pylypenko, O. et al. (2017). Oxidation of F-actin controls the terminal steps of cytokinesis. *Nat. Commun.* **8**, 14528. doi:10.1038/ncomms14528

Gatta, A. T. and Carlton, J. G. (2019). The ESCRT-machinery: closing holes and expanding roles. *Curr. Opin. Cell Biol.* **59**, 121-132. doi:10.1016/j.ceb.2019.04.005

Holder, J., Poser, E. and Barr, F. A. (2019). Getting out of mitosis: spatial and temporal control of mitotic exit and cytokinesis by PP1 and PP2A. *FEBS Lett.* **593**, 2908-2924. doi:10.1002/1873-3468.13595

Hwang, M. H., Cho, K. H., Jeong, K. J., Park, Y.-Y., Kim, J. M., Yu, S.-L., Park, C. G., Mills, G. B. and Lee, H. Y. (2017). RCP induces Slug expression and cancer cell invasion by stabilizing β1 integrin. *Oncogene* **36**, 1102-1111. doi:10.1038/onc.2016.277

Jin, M. and Goldenring, J. R. (2006). The Rab11-FIP1/RCP gene codes for multiple protein transcripts related to the plasma membrane recycling system. *Biochim. Biophys. Acta* **1759**, 281-295. doi:10.1016/j.bbaexp.2006.06.001

Jing, J., Junutula, J. R., Wu, C., Burden, J., Matern, H., Peden, A. A. and Prekeris, R. (2010). FIP1/RCP binding to Golgin-97 regulates retrograde transport from recycling endosomes to the trans-Golgi network. *Mol. Biol. Cell* **21**, 3041-3053. doi:10.1091/mbc.e10-04-0313

Klinkert, K. and Echard, A. (2016). Rab35 GTPase: a central regulator of phosphoinositides and F-actin in endocytic recycling and beyond. *Traffic* **17**, 1063-1077. doi:10.1111/tra.12422

Klinkert, K., Rocancourt, M., Houdusse, A. and Echard, A. (2016). Rab35 GTPase couples cell division with initiation of epithelial apico-basal polarity and lumen opening. *Nat. Commun.* **7**, 11166. doi:10.1038/ncomms11166

Kouranti, I., Sachse, M., Arouche, N., Goud, B. and Echard, A. (2006). Rab35 regulates an endocytic recycling pathway essential for the terminal steps of cytokinesis. *Curr. Biol.* **16**, 1719-1725. doi:10.1016/j.cub.2006.07.020

Laflamme, C., Galan, J. A., Ben El Kadhi, K., Méant, A., Zeledon, C., Carréno, S., Roux, P. P. and Emery, G. (2017). Proteomics screen identifies class I Rab11 family interacting proteins as key regulators of cytokinesis. *Mol. Cell. Biol.* **37**, e00278-16. doi:10.1128/MCB.00278-16

Lall, P., Lindsay, A. J., Hanscom, S., Kecman, T., Taglauer, E. S., Mcveigh, U. M., Franklin, E., Mccaffrey, M. W. and Khan, A. R. (2015). Structure-Function Analyses of the Interactions between Rab11 and Rab14 Small GTPases with Their Shared Effector Rab Coupling Protein (RCP). *J. Biol. Chem.* **290**, 18817-18832. doi:10.1074/jbc.M114.612366

Li, D., Kuehn, E. W. and Prekeris, R. (2014a). Kinesin-2 mediates apical endosome transport during epithelial lumen formation. *Cell Logist.* **4**, e28928. doi:10.4161/cl.28928

Li, D., Mangan, A., Cicchini, L., Margolis, B. and Prekeris, R. (2014b). FIP5 phosphorylation during mitosis regulates apical trafficking and lumenogenesis. *EMBO Rep.* **15**, 428-437. doi:10.1002/embr.201338128

Lindsay, A. J. and Mccaffrey, M. W. (2004). The C2 domains of the class I Rab11 family of interacting proteins target recycling vesicles to the plasma membrane. *J. Cell Sci.* **117**, 4365-4375. doi:10.1242/jcs.01280

Lindsay, A. J. and Mccaffrey, M. W. (2005). Purification and functional properties of Rab11-FIP2. *Methods Enzymol.* **403**, 491-499. doi:10.1016/S0076-6879(05)03043-0

Moore, R. H., Millman, E. E., Alpizar-Foster, E., Dai, W. and Knoll, B. J. (2004). Rab11 regulates the recycling and lysosome targeting of beta2-adrenergic receptors. *J. Cell Sci.* **117**, 3107-3117. doi:10.1242/jcs.01168

Nalefski, E. A. and Falke, J. J. (1996). The C2 domain calcium-binding motif: structural and functional diversity. *Protein Sci.* **5**, 2375-2390. doi:10.1002/pro.5560051201

Nedvetsky, P. I., Stefan, E., Frische, S., Santamaria, K., Wiesner, B., Valenti, G., Hammer, J. A., III, Nielsen, S., Goldenring, J. R., Rosenthal, W. et al. (2007). A Role of myosin Vb and Rab11-FIP2 in the aquaporin-2 shuttle. *Traffic* **8**, 110-123. doi:10.1111/j.1600-0854.2006.00508.x

Neto, H., Balmer, G. and Gould, G. (2013). Exocyst proteins in cytokinesis: regulation by Rab11. *Commun. Integr. Biol.* **6**, e27635. doi:10.4161/cib.27635

Peden, A. A., Schonteich, E., Chun, J., Junutula, J. R., Scheller, R. H. and Prekeris, R. (2004). The RCP-Rab11 complex regulates endocytic protein sorting. *Mol. Biol. Cell* **15**, 3530-3541. doi:10.1091/mbc.e03-12-0918

Peterman, E. and Prekeris, R. (2019). The postmitotic midbody: regulating polarity, stemness, and proliferation. *J. Cell Biol.* **218**, 3903-3911. doi:10.1083/jcb.201906148

Prekeris, R. (2011). Actin regulation during abscission: unexpected roles of Rab35 and endocytic transport. *Cell Res.* **21**, 1283-1285. doi:10.1038/cr.2011.131

Qi, M., Williams, J. A., Chu, H., Chen, X., Wang, J.-J., Ding, L., Akhirome, E., Wen, X., Lapierre, L. A., Goldenring, J. R. et al. (2013). Rab11-FIP1C and Rab14 direct plasma membrane sorting and particle incorporation of the HIV-1 envelope glycoprotein complex. *PLoS Pathog.* **9**, e1003278. doi:10.1371/journal.ppat.1003278

Rainero, E., Caswell, P. T., Muller, P. A. J., Grindlay, J., Mccaffrey, M. W., Zhang, Q., Wakelam, M. J. O., Vousden, K. H., Graziani, A. and Norman, J. C. (2012). Diacylglycerol kinase α controls RCP-dependent integrin trafficking to promote invasive migration. *J. Cell Biol.* **196**, 277-295. doi:10.1083/jcb.201109112

Sechi, S., Colotti, G., Belloni, G., Mattei, V., Frappaolo, A., Raffa, G. D., Fuller, M. T. and Giansanti, M. G. (2014). GOLPH3 is essential for contractile ring formation and Rab11 localization to the cleavage site during cytokinesis in Drosophila melanogaster. *PLoS Genet.* **10**, e1004305. doi:10.1371/journal.pgen.1004305

Sugimoto, K., Nishi, H., Miyazawa, T., Fujita, S., Okada, M. and Takemura, T. (2014). A novel OCRL1 mutation in a patient with the mild phenotype of Lowe syndrome. *Tohoku J. Exp. Med.* **232**, 163-166. doi:10.1620/tjem.232.163

Takahashi, S., Takei, T., Koga, H., Takatsu, H., Shin, H.-W. and Nakayama, K. (2011). Distinct roles of Rab11 and Arf6 in the regulation of Rab11-FIP3/arfophilin-1 localization in mitotic cells. *Genes Cells* **16**, 938-950. doi:10.1111/j.1365-2443.2011.01538.x

Vicinanza, M., Di Campli, A., Polishchuk, E., Santoro, M., Di Tullio, G., Godi, A., Levtchenko, E., De Leo, M. G., Polishchuk, R., Sandoval, L. et al. (2011). OCRL controls trafficking through early endosomes via PtdIns4,5P(2)-dependent regulation of endosomal actin. *EMBO J.* **30**, 4970-4985. doi:10.1038/emboj.2011.354

Vietri, M., Radulovic, M. and Stenmark, H. (2020). The many functions of ESCRTs. *Nat. Rev. Mol. Cell Biol.* **21**, 25-42. doi:10.1038/s41580-019-0177-4

Willenborg, C., Jing, J., Wu, C., Matern, H., Schaack, J., Burden, J. and Prekeris, R. (2011). Interaction between FIP5 and SNX18 regulates epithelial lumen formation. *J. Cell Biol.* **195**, 71-86. doi:10.1083/jcb.201011112